

Article

# Modeling of RC Moment Frame Retrofit with Mortar Walls Reinforced with Steel Wire Mesh

Melisa Herrera <sup>1,\*</sup>, Diego Sosa <sup>1</sup>, Sigfredo Díaz <sup>1</sup> and Jessica Thangjitham <sup>2</sup>

<sup>1</sup> Centro de Investigación de la Vivienda, Departamento de Ingeniería Civil y Ambiental, Escuela Politécnica Nacional, Quito 170525, Ecuador; diego.sosac@epn.edu.ec (D.S.); sigdiaz@yahoo.com (S.D.)

<sup>2</sup> School of Civil and Environmental Engineering, Georgia Institute of Technology, Atlanta, GA 30332, USA; jesthang@gatech.edu

\* Correspondence: melisa.herrera@epn.edu.ec

**Abstract:** Current construction codes require detailed analyses for structural retrofitting, which must consider performance during seismic events. Therefore, the computational models used to evaluate existing infrastructure require nonlinear structural analysis and damage estimates. For structural retrofitting, nonlinear computational modeling must represent the connectivity between existing and new elements. This study proposes recommendations on structural modeling based on fiber elements to represent reinforced concrete (RC) moment frames retrofitted with mortar walls reinforced with steel wire mesh. For this purpose, capacity curves of moment frames retrofitted with mortar walls were calculated by hand with the Bernoulli–Euler beam theory, moment–curvature analyses, and a plastic hinge model. Then, these capacity curves were used to calibrate the connectivity and constraint conditions in fiber models between the existing frame and the new wall required to capture the performance of the retrofitted structure. The study found that, for a single wall connected with top and bottom frame border elements, the capacity curves from fiber models underestimate stiffness, maximum strength, and residual strength. These estimation issues are reduced by including intermediate connectivity nodes between the top and bottom frame where rigid link constraints connect the existing frame with the new wall.

**Keywords:** fiber modeling; capacity curve; moment frame retrofit; mortar wall; steel wire mesh



**Citation:** Herrera, M.; Sosa, D.; Díaz, S.; Thangjitham, J. Modeling of RC Moment Frame Retrofit with Mortar Walls Reinforced with Steel Wire Mesh. *Appl. Sci.* **2023**, *13*, 9973. <https://doi.org/10.3390/app13179973>

Academic Editors: Konstantinos Morfidis and Konstantinos Kostinakis

Received: 20 June 2023

Revised: 28 July 2023

Accepted: 4 August 2023

Published: 4 September 2023



**Copyright:** © 2023 by the authors. Licensee MDPI, Basel, Switzerland. This article is an open access article distributed under the terms and conditions of the Creative Commons Attribution (CC BY) license (<https://creativecommons.org/licenses/by/4.0/>).

## 1. Introduction

RC moment frames are a typical lateral load-resisting system widely used for decades. Modern codes allow the use of RC moment frames in high seismic regions as long as they implement special design detailing (for example, beam–column joint design) to achieve adequate lateral resistance during a seismic event [1]. Moreover, existing infrastructure was designed with previous codes that do not meet current design requirements. Existing structures that use RC moment frame systems are very flexible, so they tend to exceed current code drift limits. Furthermore, the structural response of these flexible structures is highly influenced by masonry division panels, which increase the overall lateral frame strength and may induce local failures [2].

On the other hand, RC shear walls perform better than RC moment frames [3,4]. In a dual system (shear walls and moment frames), shear walls may prevent building damage, even though the frame elements are insufficient to support lateral loads [5]. Furthermore, shear walls reduce drifts and increase structural redundancy, but they must have sufficient strength, stiffness, and deformation capacity [6].

In addition to conventional shear walls, some variations of this system have been developed. For example, thin lightly reinforced concrete walls have been used in the last two decades to brace mid-to-high-rise buildings in some Latin American countries [7–9]. This alternative system uses walls between 80 to 100 mm thick with a single steel reinforcement layer of welded wire mesh.

Similarly to the lightly reinforced concrete walls system, an approach has been used to retrofit moment frame structures by jacketing the masonry infill panels between the frames with thin mortar walls. Some studies of moment frame systems filled with confined masonry and retrofitted mortar walls have been carried out to characterize the performance of this approach [10–13]. It has been observed that the jacketing of confined masonry with mortar walls reinforced with steel wire mesh is an effective technique for improving structural performance [10,11].

For practical applications in structural design, the retrofit of existing structures requires predictions made with nonlinear structural models that must address the connectivity between existing and new elements. Moreover, mortar walls have different material properties than frame border elements made with concrete and reinforcing steel. The new transverse wall section of the border frame columns connected by a mortar wall web, will need to consider the new material properties to reach equilibrium. Therefore, calibrating the nonlinear computational model used in the structural analysis of moment frames retrofitted with mortar walls requires a verification of the connectivity and equilibrium of the system.

This study proposes connectivity and constraint conditions for moment frame systems retrofitted with mortar walls and modeled with fiber elements with different material properties for existing and new elements. The connectivity and constraint conditions are calibrated based on benchmark capacity curves obtained by Bernoulli–Euler beam theory, moment–curvature analysis, and the plastic hinge model proposed by Priestley et al. [14]. The structural program SeismoStruct was used to develop fiber models [15], including wall aspect ratios ( $H/L_w$ ) of 1, 2, and 3.

The study found that using a single wall element to connect the top and bottom frame border elements with a rigid link constraint condition underestimates maximum strength, stiffness, and residual strength. A solution was proposed to improve the capacity prediction by including at least one intermediate connectivity node at the wall at mid-height, where the lateral columns are connected to the wall with rigid links. This approach improves the prediction of the capacity curve because it better represents the Bernoulli–Euler beam theory that plane sections must remain plain. Finally, the calibration made in this study gives guidance for nonlinear models of RC moment frames retrofitted with mortar walls, which are required for evaluating and retrofitting existing infrastructure.

### *Research Significance*

This study proposes an improved method for modeling the connectivity and constraint conditions for nonlinear fiber elements of RC moment frames retrofitted with mortar walls reinforced with steel wire mesh. The modeling results are important as they show that the capacity curves of the retrofitted wall system underestimate the maximum strength, initial stiffness, and residual strength. The underestimation of the capacity curves from the model is caused by insufficient connectivity and constraint conditions between the border frame and the mortar wall elements.

## **2. Materials and Methods**

### *2.1. Overview*

Capacity curves obtained by hand calculation were carried out with moment–curvature analyses and the plastic hinge model proposed by Priestley et al. [14]. The moment–curvature considers a composite section made of border columns (existing elements) connected to a mortar wall web (new element), so different constitutive materials are used for concrete and steel of each type of element. Moreover, the border columns with the mortar wall work together like a shear wall made of different materials. The capacity curves obtained by this approach were used as a benchmark to calibrate the required connectivity and constraint conditions of nonlinear fiber elements to represent RC moment frame systems retrofitted with mortar walls. The computational models were developed with SeismoStruct [15], and  $H/L_w$ s of 1, 2, and 3 were evaluated. For each  $H/L_w$ , a

different discretization in the wall height was considered. For example, the wall height was discretized in 2, 3, and 4 elements by including additional connectivity nodes at the border columns and the mortar wall web for each location where the wall height was divided. Moreover, the additional connectivity nodes were used to connect the border columns and the mortar wall web by including rigid links at the different sections generated by the discretization of the wall height. Finally, the computational capacity curves were compared with the benchmarks regarding strength, stiffness, strength degradation, and convergence issues.

## 2.2. Retrofit Description

The retrofit of moment frames with mortar walls is applied to frames with masonry infill panels. The masonry between the frame is used to attach layers of steel wire mesh on both sides, and a thin layer of mortar (3 to 5 cm) covers the steel wire mesh, as shown in Figure 1. This approach is not just a jacketing of the masonry, so the mortar wall must ensure the connection with all the frame elements by steel rods with sufficient development length. Since the existing elements (moment frame) and the new elements (mortar walls) provide a good connection, the system result is a shear wall made of different constitutive materials. The shear wall requires special detailing at its base because the foundation beneath also requires retrofitting to support the new conditions (shear wall instead of moment frame). This study assumes that the moment frame and mortar wall interface has sufficient steel rods to ensure connectivity (steel–concrete interface is considered perfect). Moreover, it is also assumed that the shear strength of the wall is larger than the flexural strength to prevent shear failure.

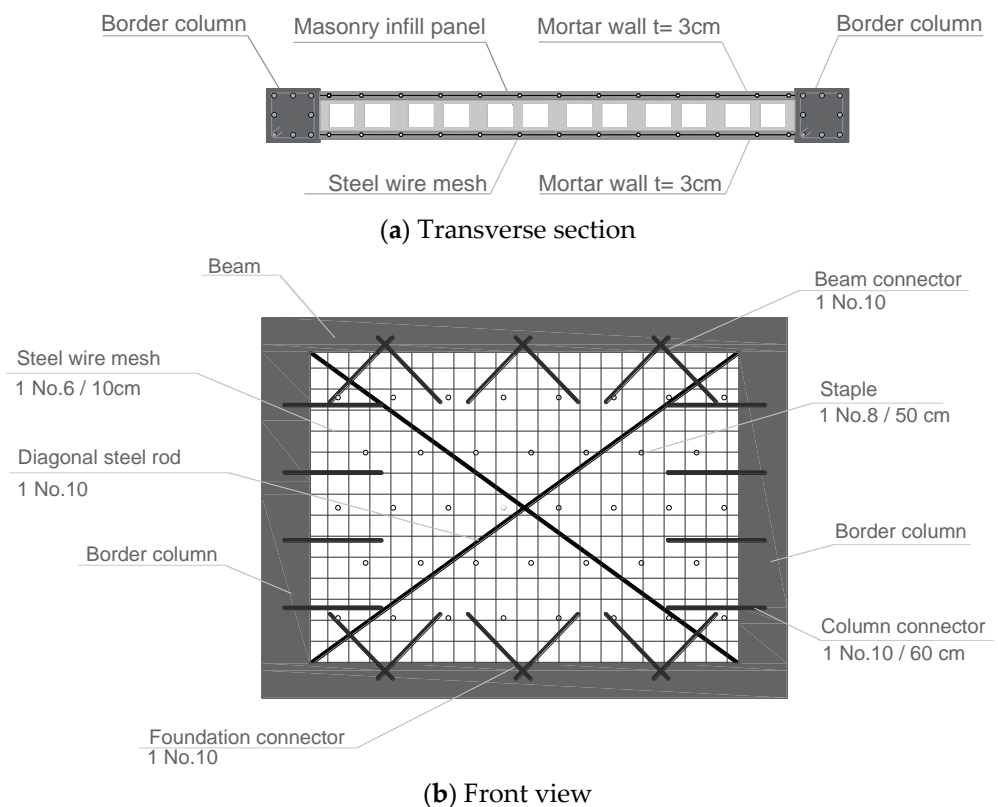


**Figure 1.** Retrofit of moment frame with mortar wall.

## 2.3. Transverse Section Geometry

The analyzed shear wall is 2.6 m in length, and three different heights were considered (2.6 m, 5.2 m, and 7.8 m). Thus, this study evaluates three different H/Lws (1, 2, and 3). The frame has 0.25 m square columns with eight No.12 longitudinal reinforcing bars.

Additionally, the columns have one No.10 stirrup every 0.1 m. The masonry infill panel was disregarded because it does not provide structural capacity; this masonry keeps the steel wire mesh in place before the mortar is cast. The influence of the masonry infill panel was evaluated by comparing cases with and without the masonry for three masonry compression strengths ( $f'm = 1 \text{ MPa}$ ,  $f'm = 10 \text{ MPa}$ , and  $f'm = 30 \text{ MPa}$ ). Structural masonry has values of  $f'm$  between 10 MPa and 30 MPa [16], but the masonry used for partition purposes has small  $f'm$  values of around 1 MPa [17]. This study focuses on non-structural masonry utilized for partition purposes. Based on the findings on the influence of masonry, which are presented in the results section of this document, the masonry infill panels were excluded from the analysis. The mortar covers a 30 mm layer at each side of the masonry, so a mortar wall of 60 mm is built between the frame elements. A steel wire mesh of 6 mm bars is spaced every 0.1 m for transverse and longitudinal reinforcement. Figure 2 summarizes the geometry for the shear wall obtained after the retrofit.



Figure 2. Transverse section geometry.

### 2.4. Material Properties

Frame elements connected by mortar wall elements work as a shear wall with different constitutive materials. For example, Figure 3 presents two constitutive materials used for steel in the composite section. The reinforcing steel used in the border frame elements is characterized by a yield stress of 420 MPa and a rupture strain of 10% (standard parameters for Grade 60 steel). On the other hand, the steel wire mesh used as reinforcement in the mortar wall has a larger yield stress of 470 MPa, but the rupture strain reduces ten times to 1%. The characteristic values presented in Figure 3 were obtained experimentally for typical steel materials available commercially. The experimental constitutive steel materials were approximated with bilinear functions as presented in Figure 3 for simplicity.

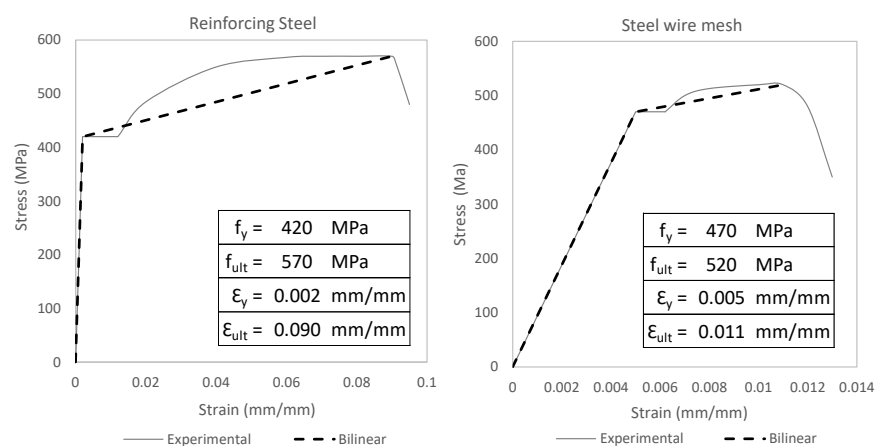
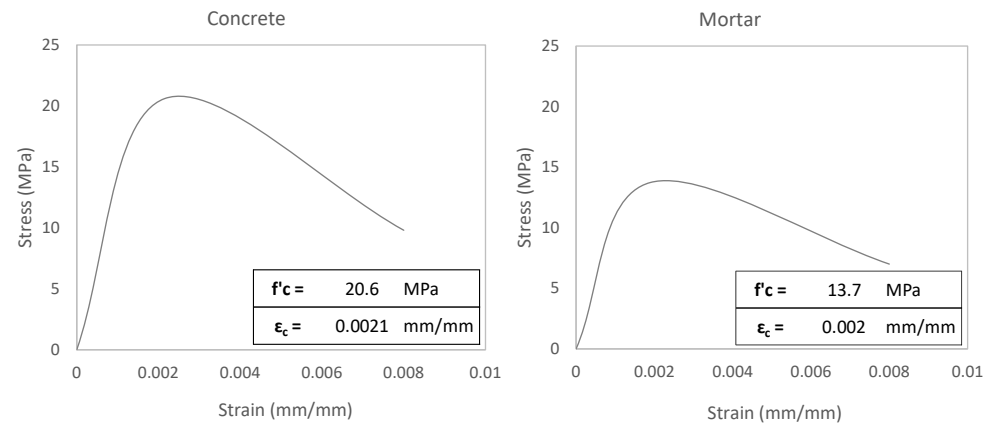


Figure 3. Steel constitutive models.

Similarly, the concrete material differs for frame elements and the mortar wall (see Figure 4). The concrete material for the border frame elements has a higher maximum compression stress ( $f'c$ ) than the mortar wall web; a typical value of 20.6 MPa was considered in this study. Due to the construction process, the concrete used to cover the masonry infill panels cannot have coarse aggregates. Thus, the material is more mortar-like than typical concrete and results in lower  $f'c$  values (an  $f'c$  of 13.7 MPa was used in this study). The

concrete elastic modulus ( $E_c$ ) also differs depending on the  $f'_c$ . For example, in this study, the  $E_c$  was 19,185 MPa for the frame elements and 14,504 MPa for the mortar walls.



**Figure 4.** Concrete and mortar constitutive models.

### 2.5. Moment–Curvature Analysis

The moment–curvature analysis considers the transverse section presented in Figure 2. The constitutive materials shown in Figure 3 are used for steel. Additionally, the concrete has an elastic response before steel yielding (see Figure 4). On the other hand, after steel yielding, the concrete stress is represented by Whitney’s compression block. The values of  $f'_c$  and  $E_c$  for concrete and mortar were outlined in the previous section.

The moment–curvature relationship is obtained by hand calculations. The neutral axis depth ( $c$ ) is determined iteratively by reaching the equilibrium of internal forces for different levels of strain demand. In the moment–curvature analysis, the strain distribution of the transverse section follows the Bernoulli–Euler beam theory (the plain sections remain plain). For the calculations, three damage levels were considered that corresponded to longitudinal steel reinforcement strain demand [14]: yield, serviceability, and damage control. Moreover, two additional strains are included to soften the moment–curvature plot. The first (Control Strain 1) is an intermediate strain between yield and serviceability, and the second (Control Strain 2) is an intermediate strain between serviceability and damage control.

The calculation procedure for curvature includes the following steps: (1) a strain demand is considered; (2) a neutral axis depth ( $c$ ) is assumed; (3) the strain distribution, as shown in Figure 5, is calculated with

$$\varepsilon_i = \frac{\varepsilon_{LS}}{d - c}(x_i - c) \quad (1)$$

where  $x_i$  is a specific location in the transverse section from the edge with the maximum compression,  $\varepsilon_i$  is the section strain at  $x_i$ ,  $\varepsilon_{LS}$  is the strain limit state,  $d$  is the section’s effective height (distance from the most compressed fiber to the further steel layer in tension),  $c$  is the neutral axis depth; (4) the internal forces (concrete compression ( $C_c$ ), steel compression ( $C_s$ ), steel tension ( $T_s$ ), and axial compression reaction ( $P$ )) are calculated based on strain distribution and constitutive material properties; (5) the equilibrium of internal forces is verified ( $C_c + C_s \approx T_s + P$ ); (6) the calculation from step 2 through step 5 is repeated until the equilibrium is satisfied; and (7) the curvature is calculated as the strain distribution rate with

$$\varnothing_{LS} = \frac{\varepsilon_{LS}}{d - c} \quad (2)$$

where  $\varnothing_{LS}$  is the curvature at a specific damage state or limit state.

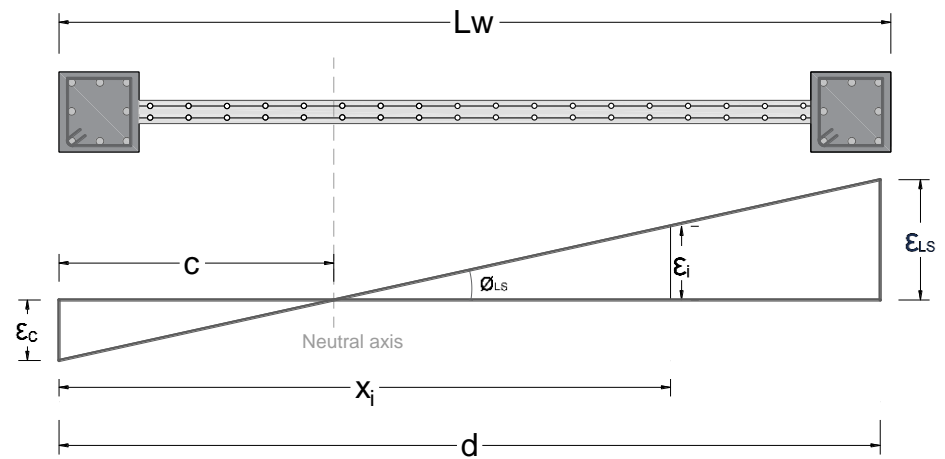


Figure 5. Strain distribution.

As presented in Figures 6 and 7, the internal forces are calculated with elastic material properties before steel yielding and with plastic material properties afterward. Moreover, Figure 6 describes the cases when the neutral axis at steel yielding ( $c_y$ ) is larger or smaller than the column section's height ( $t_f$ ). Similarly, Figure 7 indicates the two possible stress distributions in the transverse composite section for materials in the plastic range depending on the length of  $c$ . Once the equilibrium of internal forces is achieved by iterations, the distribution of stresses and forces presented in Figures 6 and 7 is used to determine the internal moment of the composite wall section.

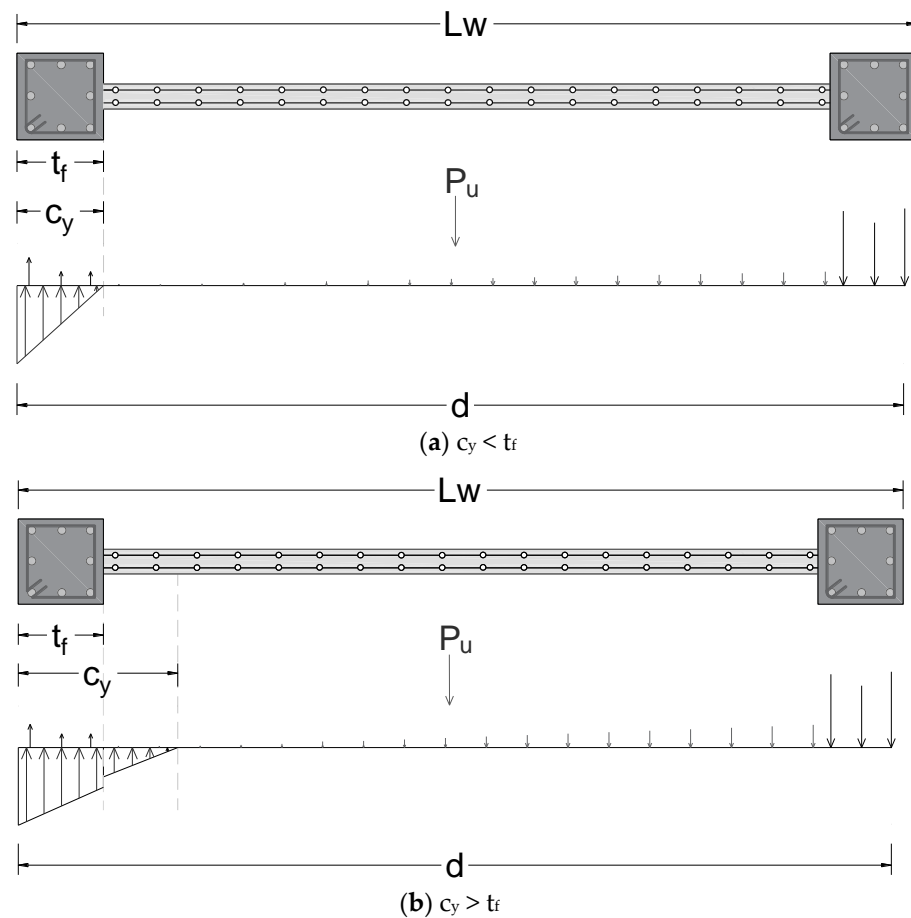


Figure 6. Internal forces for elastic range.

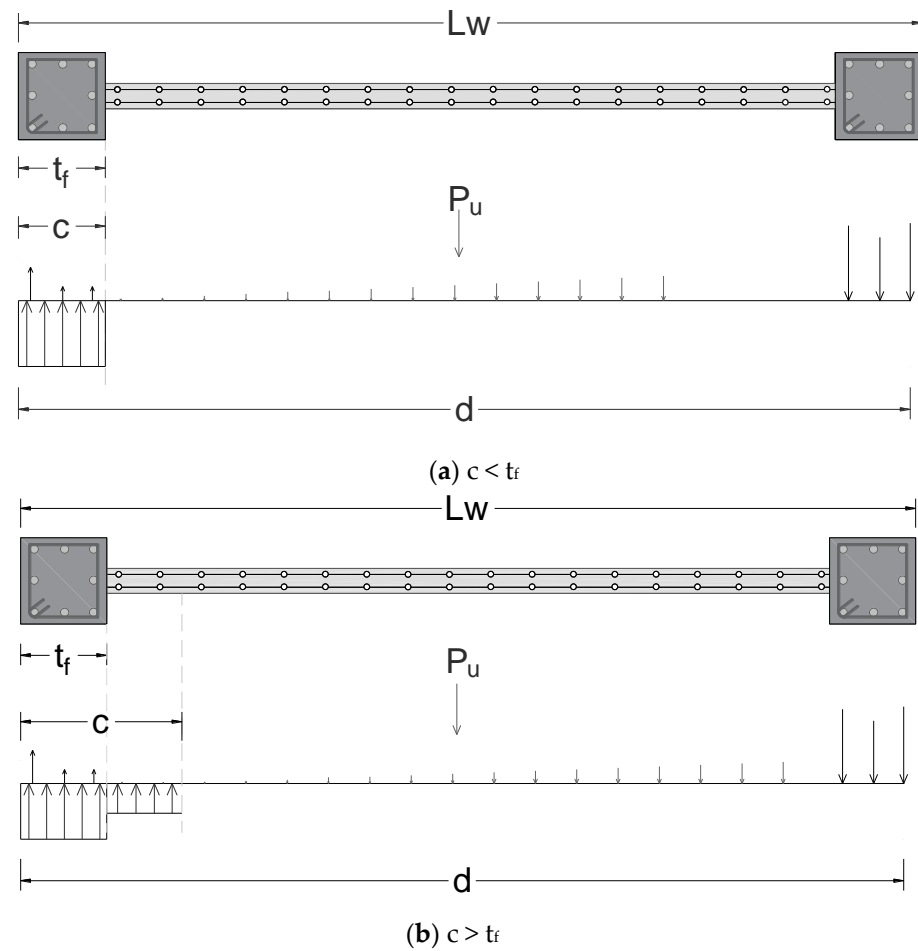


Figure 7. Internal forces for plastic range.

### 2.6. Calculation of Benchmarks Capacity Curves

With the information of the curvature ( $\phi$ ) at different damage states (yield ( $\phi_y$ ), serviceability( $\phi_s$ ), and damage control( $\phi_{DC}$ )), this study uses the plastic hinge model proposed by Priestley et al. [14] (see Figure 8) to calculate benchmark capacity curves. The curvature for a specific damage state ( $\phi_{LS}$ ) corresponds to the curvature at the wall base, and it has an elastic component known as the yield curvature ( $\phi_y$ ) and a plastic component ( $\phi_p$ ). Priestley et al. [14] simplified the actual curvature distribution to a triangle elastic and a rectangle plastic curvature distribution, as presented in Figure 8. The rectangular curvature distribution corresponds to a plastic hinge model with a plastic hinge length ( $L_p$ ) calculated with

$$L_p = k * H_e + 0.1 * L_w + L_{sp} \tag{3}$$

$$k = 0.2 * \left( \frac{f_u}{f_y} - 1 \right) \leq 0.08 \tag{4}$$

$$L_{sp} = 0.022 * f_{ye} * d_{bl} \tag{5}$$

$$H_e = 0.75 * H \tag{6}$$

where  $L_p$  is the plastic hinge length,  $H_e$  is the effective wall height,  $L_w$  is the wall length,  $L_{sp}$  is the length of strain penetration into the foundation,  $f_u$  is the steel ultimate strength,  $f_y$  is the steel yield strength,  $d_{bl}$  is the steel reinforcing diameter, and  $H$  is the wall height.

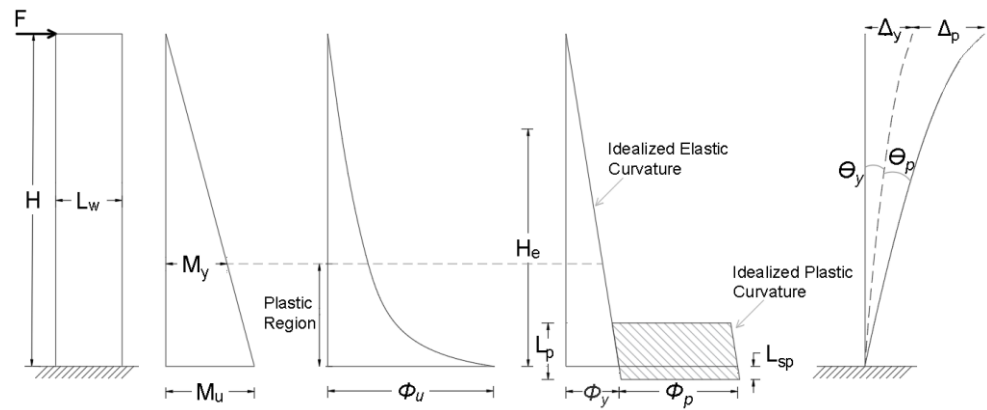


Figure 8. Curvature distribution idealization.

Using the simplified curvature distribution and Mohr’s second theorem, the lateral displacement at the top of the wall is calculated with

$$\Delta_{LS} = \Delta_y + \Delta_p \tag{7}$$

$$\Delta_y = \frac{\varnothing_y * (H + L_{sp})^2}{3} \tag{8}$$

$$\Delta_p = L_p * \varnothing_p * H \tag{9}$$

where  $\Delta_{LS}$  is the lateral displacement corresponding to a limit state,  $\Delta_y$  is the elastic displacement at the top of the wall, and  $\Delta_p$  is the plastic displacement at the top of the wall.

The plastic hinge model proposed by Priestley et al. [14] does not consider shear deformations. As presented in Figure 8, this model considers bending deformations based on curvature distribution. The current study covers mortar walls with shear strength larger than flexural strength, so shear failure is prevented (it is assumed that shear deformations are elastic at the mortar wall web). Therefore, after forming the plastic hinge at the wall base, the shear contribution is reduced gradually compared with the bending contribution. The influence of bending and shear deformations was evaluated for different aspect ratios and different displacement ductilities ( $\mu_d$ ) to assess their contribution to the wall displacement at the top ( $\Delta$ ). This displacement, which considers bending and shear deformations, was calculated with

$$\Delta = \Delta_b + \Delta_s \tag{10}$$

$$\Delta_b = \Delta_{LS} = \Delta_y + \Delta_p \tag{11}$$

$$\Delta_s = \frac{6}{5} * \frac{H}{G * A} * F \tag{12}$$

where  $\Delta$  is the wall displacement at the top (includes bending and shear contributions);  $\Delta_b$  is the bending contribution, which is the same as  $\Delta_{LS}$ ;  $\Delta_s$  is the elastic shear displacement contribution;  $G$  is the shear modulus;  $A$  is the mortar wall web transverse section; and  $F$  is the lateral strength.

The mortar wall web is the only element considered in the shear deformation contribution since this study assumes this element has sufficient shear strength to prevent shear failure. On the other hand, the masonry in the web is not considered because it has a shear failure at small drift values. For example, low-strength lightweight masonry infill panels would reach shear failure at story drifts around 0.005 [14].

Since the shear deformation is assumed elastic for this study (see Equation (12)), this component would be constant for benchmark and computational capacity curves. Therefore, in the following sections, the comparisons exclude the influence of shear deformations and only focus on the bending contribution.

### 2.7. Validation of Benchmark Capacity Curves with Experimental Results

The plastic hinge model proposed by Priestley et al. [14] is an analytical model calibrated with experimental data for standard cases such as shear walls, columns, beams, and bridge piles. However, the shear wall of this study is the result of a concrete moment frame retrofit, which has different materials for the border elements and the wall web. Therefore, the reliability of this analytical model is evaluated with an experimental test developed by Albuja and Pantoja [18] at Centro de Investigación de la Vivienda from Escuela Politécnica Nacional (CIV-EPN). Figure 9 presents the experimental test construction made by Albuja and Pantoja [18].

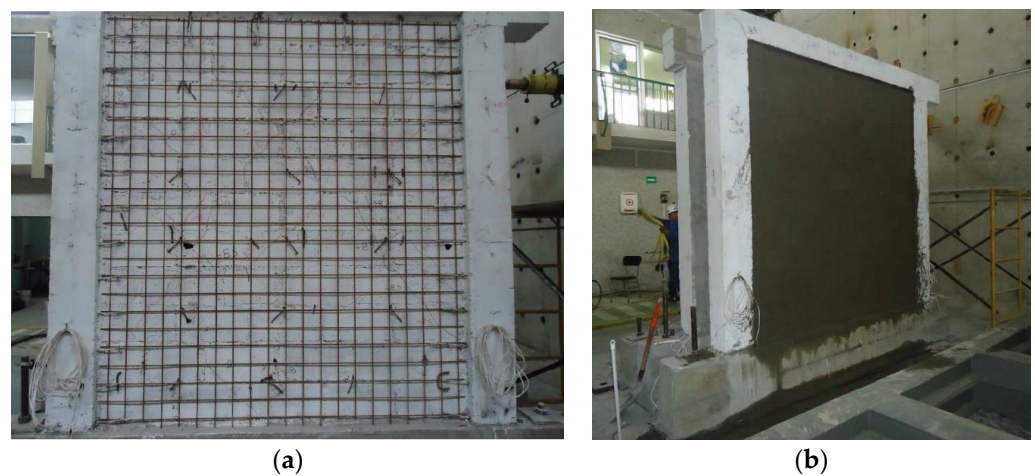


**Figure 9.** Experimental test construction details [18]. (a) Wire mesh connected by steel rods to border columns. (b) Wire mesh covered with mortar.

The experimental test provided by Albuja and Pantoja [18] uses the retrofit described in this study. Still, the moment frame and the wall web connectivity was made just at the column–wall interface (there are steel rods just at the column–wall interface). Despite this test having steel wire mesh with horizontal and vertical wires, the vertical wires do not contribute to the transverse section (see Figure 10a). For example, the absence of steel rods at the base and top of the retrofit does not provide enough development length to produce vertical wire tension. Therefore, the longitudinal steel reinforcement contributing to the wall's flexural strength is at the border columns (see Figure 10a). Finally, the benchmark and the experimental capacity curves are compared based on the maximum strength, stiffness, and residual strength. This comparison supports utilizing the analytical benchmark capacity curves without experimental data for computational model calibration.

### 2.8. Computational Fiber Models

SeismoStruct, a finite element package capable of predicting the behavior of large displacements, was used for mathematical modeling. Large displacements produce damage concentration in the spatial frames under a static or dynamic load. Additionally, SeismoStruct considers both geometric nonlinearities and material inelasticity [15].

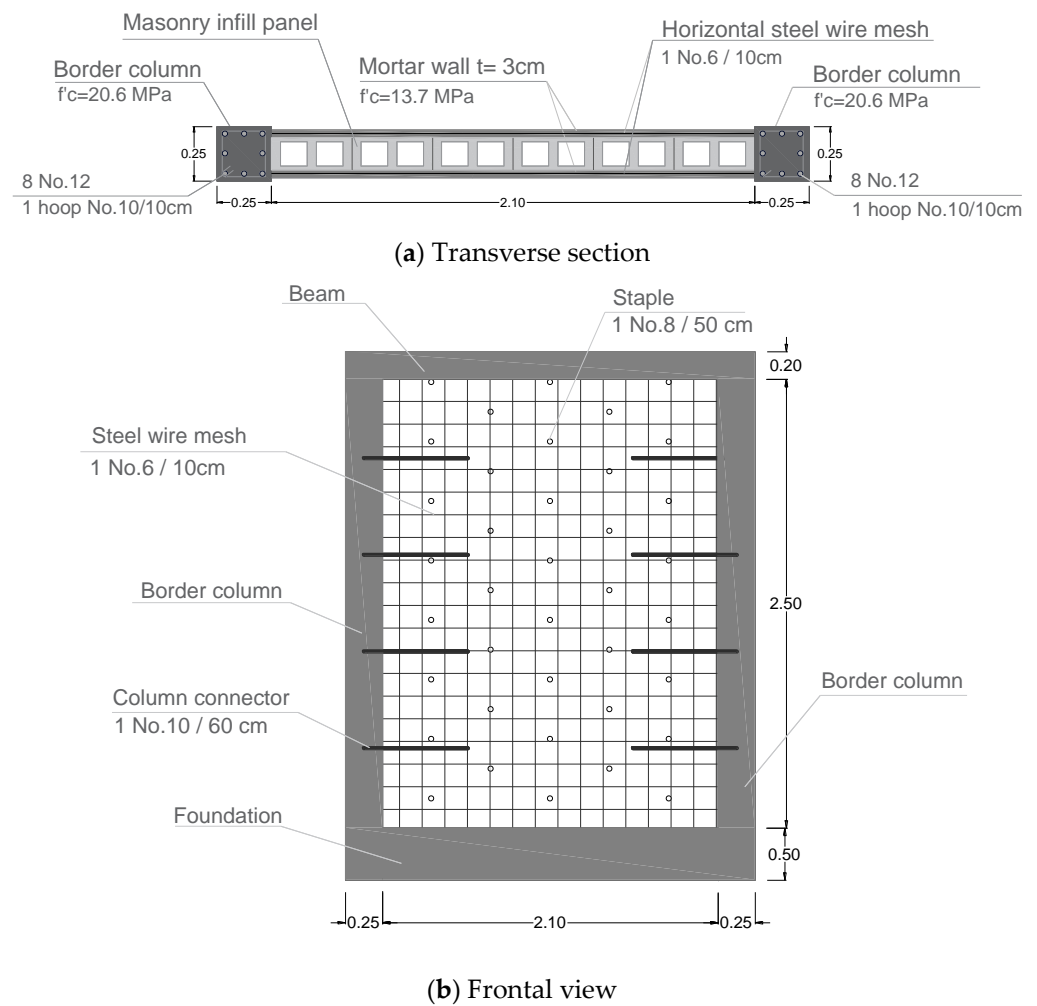


Figure 10. Experimental specimen detailing.

2.8.1. Materials

A uniaxial nonlinear model with constant confinement has been considered for the concrete constitutive model, which follows the constitutive relationship proposed by Mander et al. [19] and cyclic rules proposed by Martinez-Rueda and Elnashai [20]. The confining effects provided by lateral transverse reinforcement are incorporated using rules proposed by Mander et al. [19]. These rules assume a constant confining pressure throughout the stress–strain range [15].

Five parameters are required to define the concrete constitutive model in SeismoStruct. These parameters are compressive strength ( $f'c$ ), tensile strength ( $ft$ ), modulus of elasticity ( $Ec$ ), strain at peak stress ( $\epsilon_c$ ), and specific weight ( $Y$ ) (see Table 1). The parameters presented in Table 1 are the same values used in calculating the benchmark capacity curves.

Table 1. Concrete constitutive model parameters used in SeismoStruct.

Parameter	Column’s Concrete		Mortar Cover	
	Value	Unit	Value	Unit
$f'c$	20,593.96	kPa	13,729.31	kPa
$ft$	2059.39	kPa	1372.93	kPa
$Ec$	19,185,101.16	kPa	14,504,230.95	kPa
$\epsilon_c$	0.0021	m/m	0.0019	m/m
$Y$	24.00	kN/m <sup>3</sup>	24.00	kN/m <sup>3</sup>

For the steel constitutive material, SeismoStruct includes the Menegotto–Pinto model [21]. Table 2 includes the parameters used in SeismoStruct to define the steel constitutive model. These parameters are modulus of elasticity ( $E_s$ ), yield stress ( $f_y$ ), strain hardening parameter ( $\mu$ ), initial shape parameter of the transition curve ( $R_0$ ), calibration coefficients of the shape of the transition curve ( $a_1$ ;  $a_2$ ), calibration coefficients of isotropic hardening ( $a_3$ ;  $a_4$ ), fracture/buckling strain ( $\epsilon_{ult}$ ), and the specific weight ( $\gamma$ ).

Table 2. Steel parameters.

Parameter	Steel Reinforcement		Steel Wire Mesh	
	Value	Unit	Value	Unit
$E_s$	210,000,000.00	kPa	94,000,000.00	kPa
$f_y$	420,000.00	kPa	470,000.00	kPa
$\mu$	0.01	-	0.09	-
$R_0$	20.00	-	20.00	-
$a_1$	18.50	-	18.50	-
$a_2$	0.15	-	0.15	-
$a_3$	0.00	-	0.00	-
$a_4$	1.00	-	1.00	-
$\epsilon_{ult}$	0.09	-	0.01	-
$\gamma$	78.00	kN/m <sup>3</sup>	78.00	kN/m <sup>3</sup>

### 2.8.2. Elements

The inelastic force-based plastic hinge frame element type (infrmFBPH), available in SeismoStruct, was considered. This force-based 3D beam–column element is capable of modeling space frame members with geometric and material nonlinearities. Moreover, this element includes Gauss–Lobatto integration sections throughout its length to distribute the inelastic response (see Figure 11). The integration sections are discretized in fibers that have a uniaxial response based on the constitutive materials considered in the analysis. For example, the sectional stress–strain state of beam–column elements is obtained by integrating the nonlinear uniaxial material response of the individual fibers at each section. Furthermore, the infrmFBPH element concentrates the inelasticity within a fixed length at each end of the element, so this element type reduces analysis time and convergence issues [15].

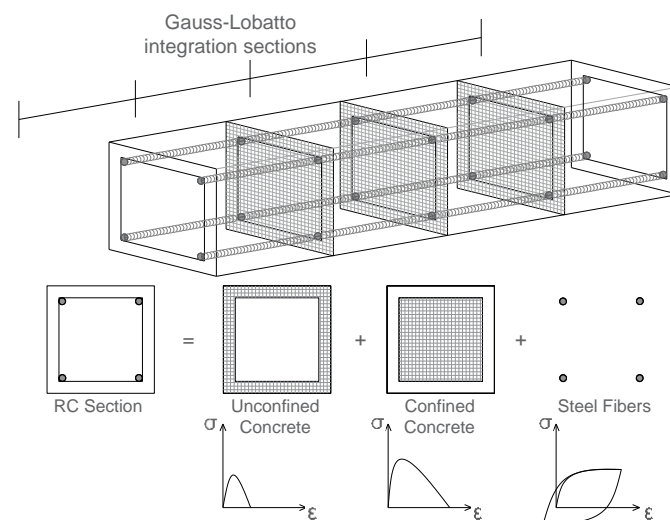


Figure 11. Gauss–Lobatto integration sections.

### 2.8.3. Fiber Transverse Sections

SeismoStruct has no composite section option to define different material properties in a wall fiber transverse section. Therefore, the border element (frame) and the web (mortar wall) sections are defined individually, as presented in Figure 12. The geometry, concrete materials, and steel reinforcement materials (transverse and longitudinal) used in the computational model sections are the same as in the benchmark capacity curve calculation (Figure 2). For example, Figure 12a shows that the border columns consider a cover (unconfined concrete), core (confined concrete), and steel reinforcement. On the other hand, Figure 12b indicates that the wall has mortar (unconfined concrete) and steel wire mesh. The number of fibers used in the integration sections was 58 for the border columns and 98 for the web mortar wall (program default discretization).

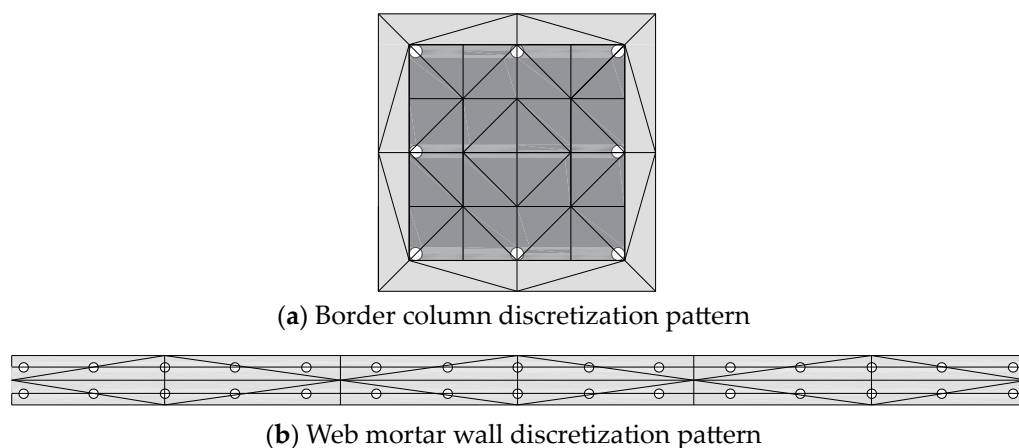


Figure 12. Cross-section discretization pattern.

### 2.8.4. Plastic Hinge Length

As mentioned before, infrmFBPH elements concentrate the inelastic response at the ends of the element. Therefore, this type of element has plastic curvature concentration at the locations of the element’s highest demands, and the plastic curvature distribution length can be calculated with the plastic hinge length model proposed by Priestley et al. model [14]. In SeismoStruct, this length is specified as a percentage of the wall height and was calculated with Equation (3). Table 3 summarizes the calculation of plastic hinge length for the three H/Lws utilized in this study.

Table 3. Plastic hinge length.

Parameter	Unit	H/Lw=1	H/Lw=2	H/Lw=3
H	m	2.600	5.200	7.800
He	m	1.950	3.900	5.850
fye	MPa	420.000	420.000	420.000
fu	MPa	570.000	570.000	570.000
dbl	m	0.012	0.012	0.012
Lsp	m	0.111	0.111	0.111
k	-	0.071	0.071	0.071
Lw	m	2.600	2.600	2.600
Lp	m	0.510	0.649	0.789
Lp	%	19.622	12.489	10.112

### 2.8.5. Constraints

Since border columns and the web mortar wall become one element, which works as a shear wall after retrofitting, the computational model must represent the inelastic response of the composite section of the new element (shear wall). In computational programs, the walls and the border columns are connected by rigid link constraints. For example,

the SeismoStruct default connection option uses one rigid link constraint at the top of the elements. Additional constraint conditions are included for calibration purposes to improve capacity curve estimations.

For this matter, the elements are discretized throughout the height to include additional connectivity nodes for defining intermediate rigid link constraints between the top and bottom of the wall. For example, Figure 13 presents discretization 1, corresponding to one intermediate rigid link constraint. For discretization 1, the border columns and the web mortar wall are discretized in the middle to provide connectivity nodes for the constraint definitions. As presented in Figure 13, the nodes at mid-height are used to define an additional rigid link constraint. The wall nodes are master nodes, and the nodes at the border columns are slave nodes (Figure 13). Similarly, two other discretization methods, discretization 2 (two intermediate rigid links) and discretization 3 (three intermediate rigid links), were evaluated in this study as presented in Figure 14.

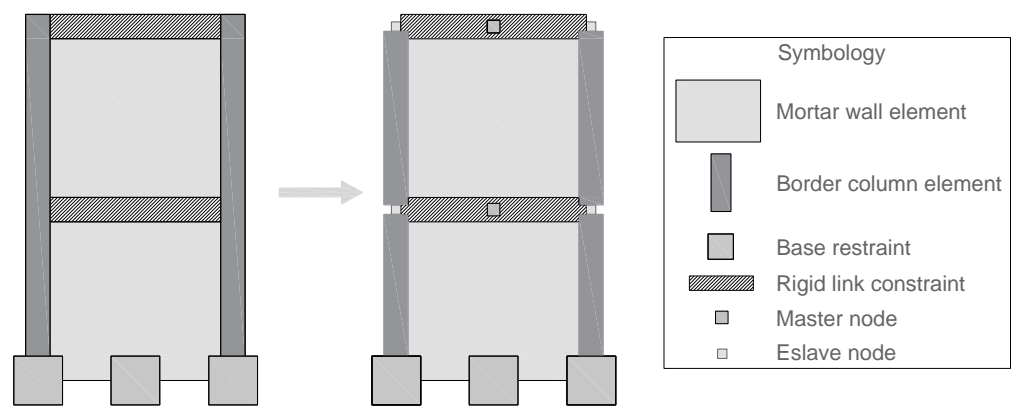


Figure 13. Discretization 1 connectivity.

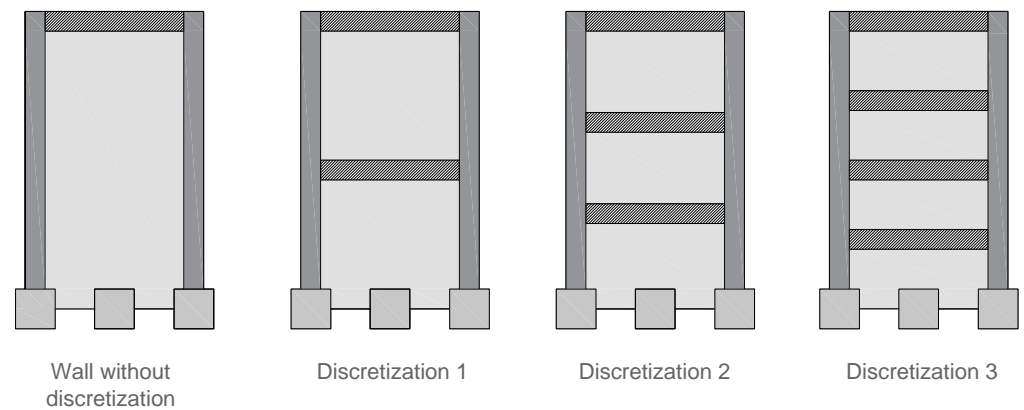


Figure 14. Wall discretization methods.

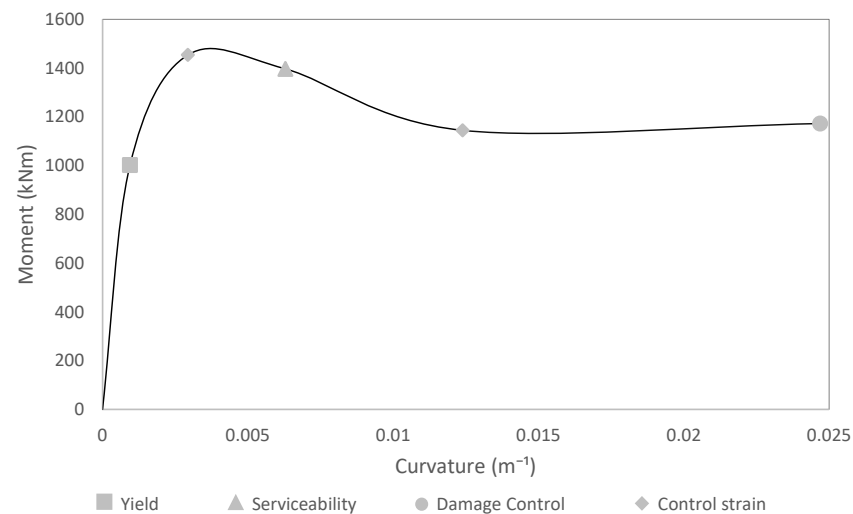
### 3. Results

#### 3.1. Moment–Curvature Diagram

Table 4 summarizes the five moment–curvature coordinates ( $M, \varnothing$ ) used to plot the moment–curvature diagram for the transverse section described in Figure 2. Each coordinate has a corresponding damage state, tension steel strain, neutral axis depth, and internal force equilibrium. Two intermediate analysis points (control strains) were included between limit states to soften the moment–curvature diagram. Figure 15 presents the moment–curvature diagram obtained by plotting the five ( $M, \varnothing$ ) coordinates presented in Table 4.

**Table 4.** Results from the moment–curvature analysis.

Strain Demand	Steel Strain	Neutral Axis Depth	Compression Forces	Tension Forces	Curvature	Moment
	( $\epsilon_s$ )	(c)	( $C_c + C_s$ )	( $T_s + P$ )	( $\emptyset$ )	(M)
	(mm/mm)	(m)	(kN)	(kN)	( $m^{-1}$ )	(kN·m)
Yield	0.002	0.456	−453.087	453.135	0.001	1001.310
Control Strain 1	0.007	0.189	−743.581	743.522	0.003	1453.210
Serviceability	0.015	0.188	−789.483	789.565	0.006	1395.970
Control Strain 2	0.030	0.149	−673.590	673.670	0.012	1144.380
Damage control	0.060	0.140	−682.646	682.594	0.025	1172.280

**Figure 15.** Moment–curvature diagram.

The shear wall (the border columns combined with the mortar wall) reaches a maximum strength between the steel yielding and serviceability limit state, and the serviceability limit state occurs at the initiation of strength degradation. This behavior is unlike that of conventional RC shear walls (walls with the same material at the border and web sections). In the case of RC moment frames retrofitted with mortar walls and steel wire mesh, the mortar will crush first, and the steel wire mesh will fracture first. However, the frame elements can sustain larger strains before being damaged, and they are the primary supporting system. Moreover, the mortar wall is an element that can be replaced easily, so the limit states in this study correspond to the materials used in the moment frame system.

Since the steel wire mesh fractures ten times earlier than the steel reinforcement, the strength degradation initiates with the fracture of the steel wire mesh (longitudinal wires). However, the strength stabilizes after the fracture of most of the longitudinal wires located close to the border columns. After this condition, the strength is sustained mainly by the steel reinforcement of the border columns. Figure 15 shows that the damage control limit state may be reached after strength stabilizes. Still, this behavior is possible only if the mortar wall reinforced with steel wire mesh does not experience shear failure.

### 3.2. Benchmarks Capacity Curves

The benchmark capacity curves were calculated with the moment–curvature diagram presented in Figure 15 and the plastic hinge model proposed by Priestley et al. [14]. Figure 15 is the same for all the H/Lws considered in this study, but the capacity curves differ for each case. For example, Figure 16 shows the benchmark capacity curves for each H/Lw. It can be seen that a higher H/Lw (flexible walls) corresponds to lower lateral strength and initial stiffness but has a larger displacement capacity. On the other hand, short walls (H/Lw = 1) have the largest strength and initial stiffness, but the displacement

capacity reduces. Additionally, the wall with  $H/L_w = 1$  has the largest drop from the maximum strength to residual strength, while the wall with  $H/L_w = 3$  has a softer transition from the maximum strength to residual strength. As mentioned, the capacity curves can reach a lateral displacement corresponding to the damage control limit state only if the wall does not experience shear failure. Thus, a detailed capacity design of the wall must be carried out to avoid undesirable failure modes like shear failure.

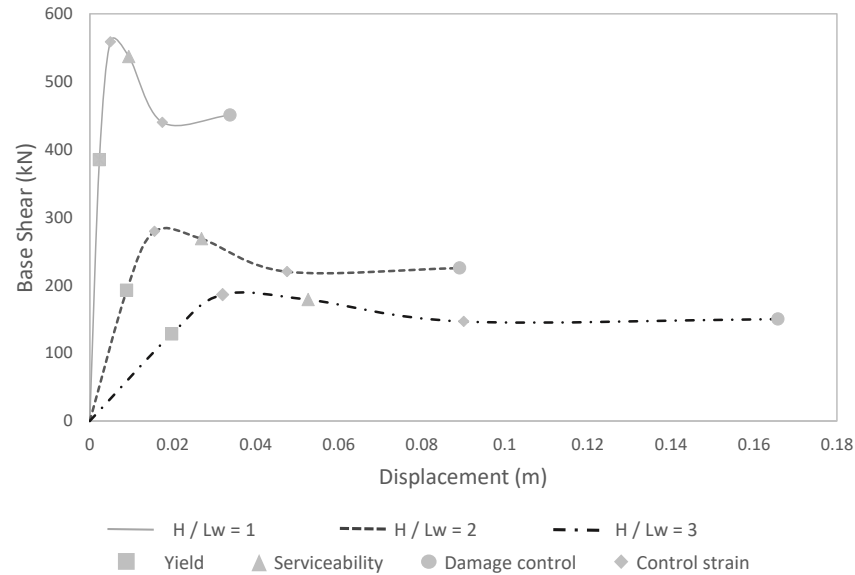


Figure 16. Benchmark capacity curves.

### 3.2.1. Shear Deformation Influence

Figure 17 compares capacity curves with and without the influence of shear deformations. The case of  $H/L_w = 1$  is the most sensitive, and the case of  $H/L_w = 3$  is the least sensitive. As mentioned, the mortar wall web is the only element considered in verifying shear deformation influence since this study assumes that this element has sufficient shear strength to prevent shear failure.

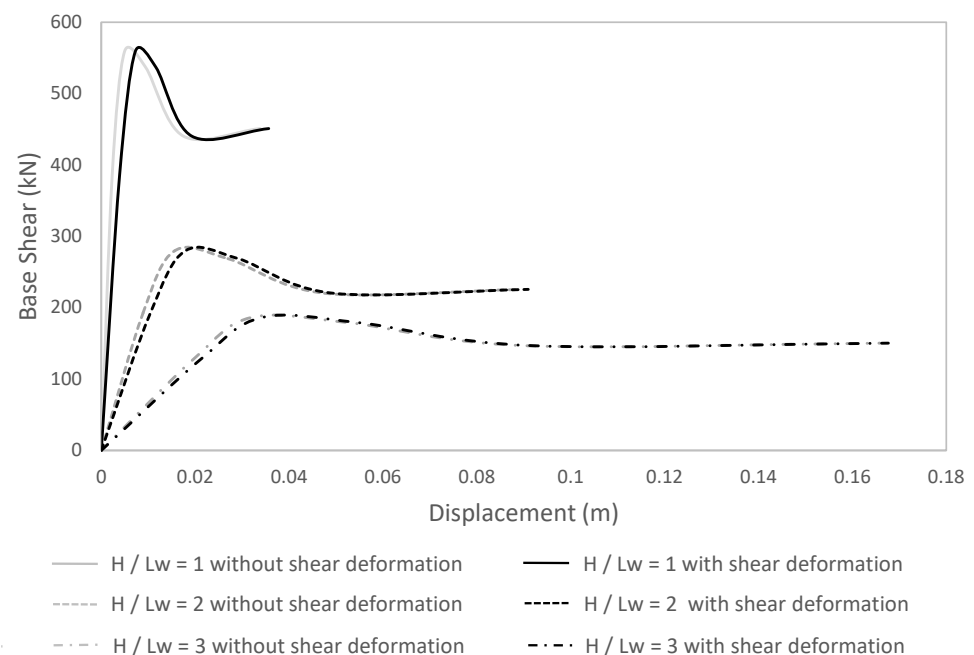


Figure 17. Shear deformation influence in capacity curves.

This study addresses cases where shear failure does not occur (shear strength > flexural strength), and the shear deformation is assumed elastic. Figure 18 compares the bending and shear deformation contributions in the wall top displacement for different  $\mu_d$  and H/Lw values from short to tall walls. As expected, the displacement in short walls has a larger shear deformation contribution (especially for small displacements). For example, Figure 18 shows that shear deformation contributes 41% of the total displacement for the wall with H/Lw = 1 (short wall) and  $\mu_d = 1$  (small displacements), and this percentage reduces to 15% and 7% for H/Lw = 2 and H/Lw = 3, respectively.

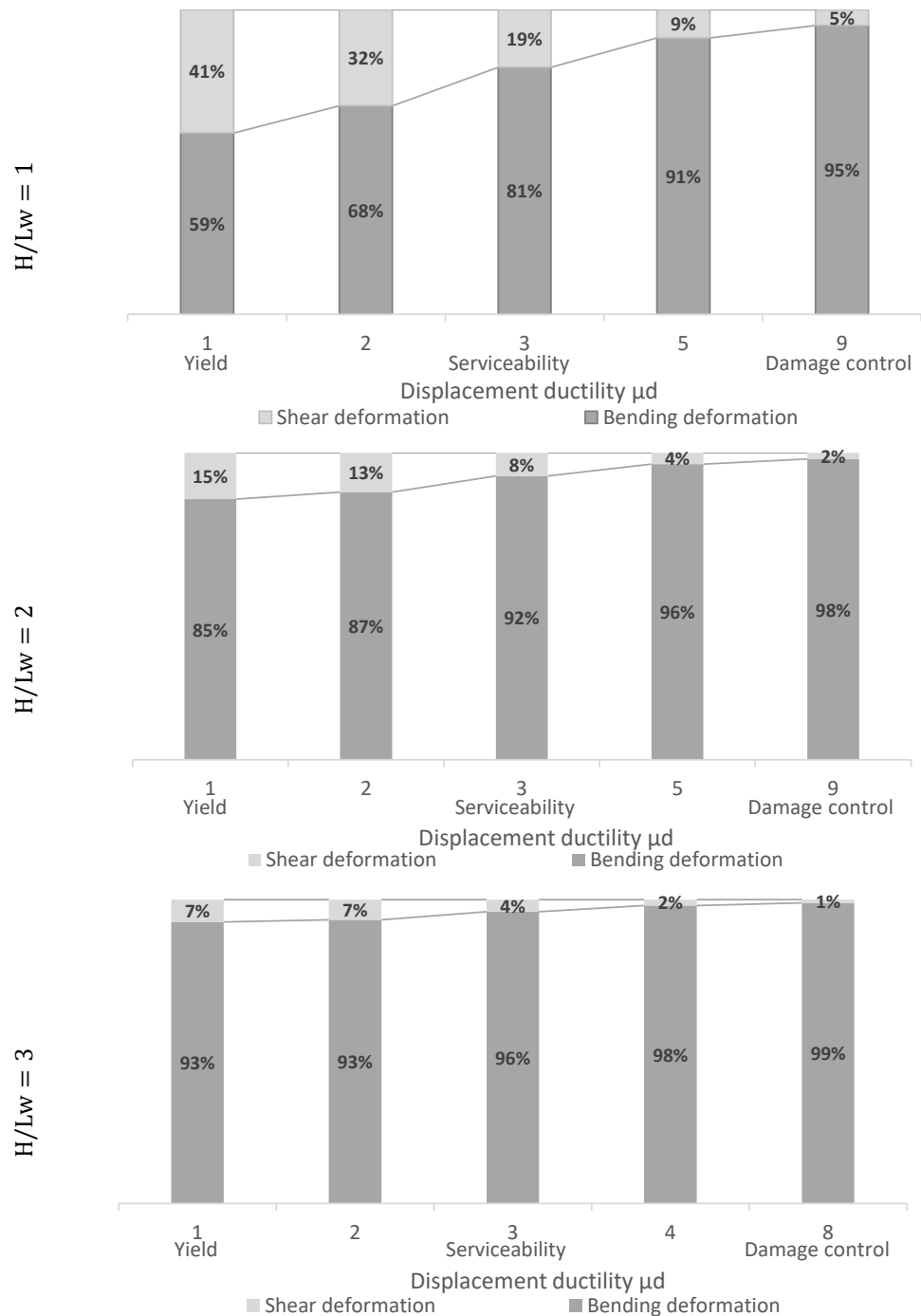


Figure 18. Flexural vs. shear displacement contribution.

Moreover, shear displacement components reduce with the increment of  $\mu_d$ . For example, Figure 18 shows that the short wall reduces the shear deformation contribution in the wall displacement from 41% to 5%. Similarly, the walls with  $H/Lw = 2$  and  $H/Lw = 3$  reduce the shear contribution from 15% to 2% and 7% to 1%, respectively. Once the displacement includes a plastic component from the plastic hinge at the wall base, the flexural contribution increases its influence (see Figure 18).

### 3.2.2. Masonry Infill Panels Contribution

The benchmark capacity curves presented in Figure 19 include cases with and without the influence of masonry. The masonry was implemented in calculating the benchmark capacity curves by including an effective additional area in the wall web with three different  $f'm$  values (1 MPa, 10 MPa, and 30 MPa). The masonry may contribute to the flexural strength of the wall. However, the masonry has a shear failure at small displacements, and this study focuses on large displacements where the plastic hinge is developed at the wall base. Therefore, it is assumed that the masonry does not contribute to shear deformations for  $\mu_d > 1$ , but the influence on the flexural strength may be evaluated.

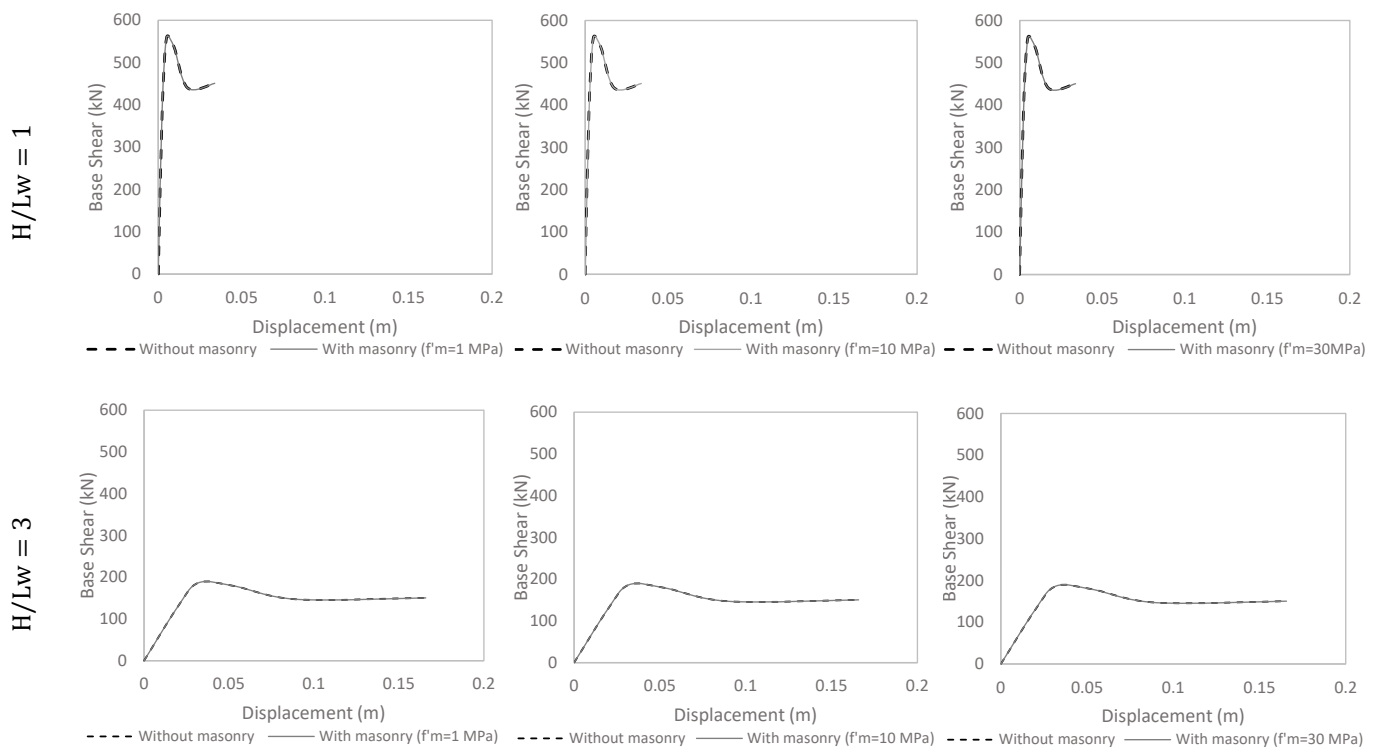


Figure 19. Infill panel masonry contribution in benchmark capacity curves.

Figure 19 presents the benchmark capacity curves with and without masonry, and it is observed that masonry does not influence the capacity curve for short and tall walls (capacity curves coincide with each other). While performing the moment–curvature analysis for the wall, the neutral axis depth is observed to be larger than the column height ( $c > tf$ ) for the yielding limit state. Therefore, for small displacements, the masonry contributes to flexural strength (see Figure 20a). On the other hand, for large displacements, the neutral axis depth is smaller than the column height ( $c < tf$ ), so masonry does not contribute (see Figure 20b). Table 5 presents numerical values of this variation, and it is observed that the influence is insignificant for maximum flexural strength, stiffness, and residual strength. Therefore, it is recommended to disregard the masonry when modeling.

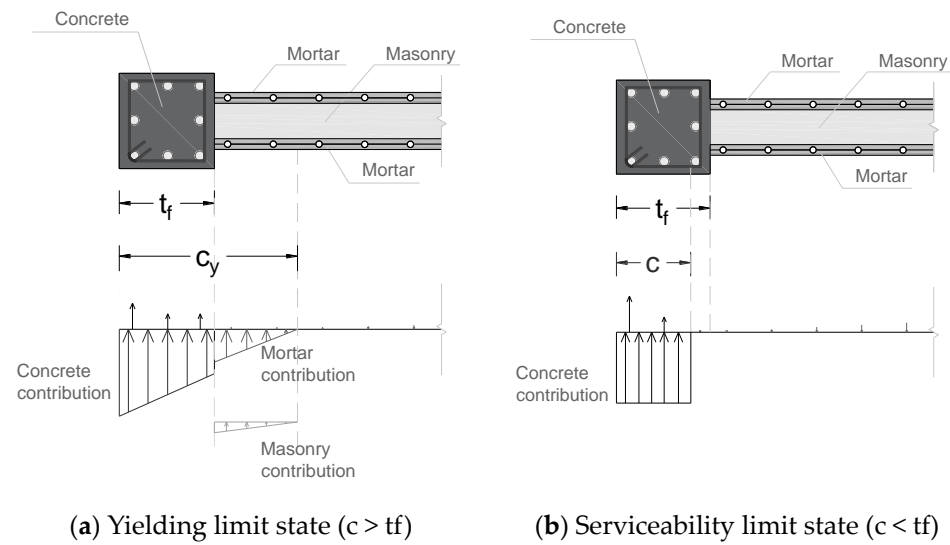


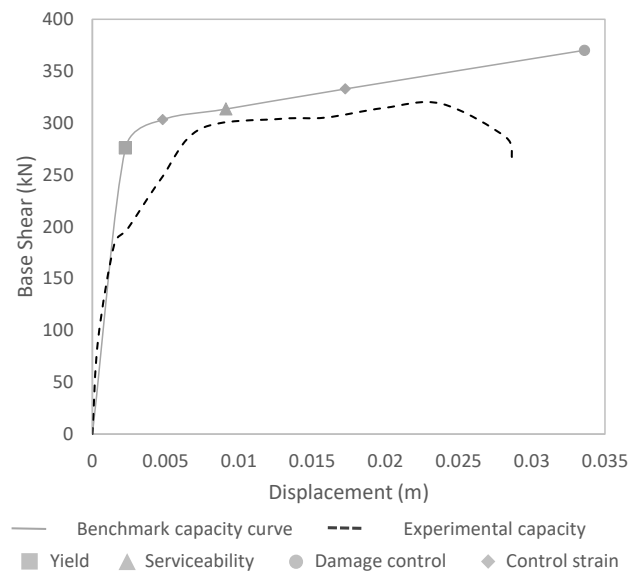
Figure 20. Masonry stress contribution for yielding and serviceability limit states.

Table 5. Infill panel masonry contribution based on maximum strength, stiffness, and residual strength.

Case of Study	Maximum Strength	Error	Stiffness	Error	Residual Strength	Error	
	(kN)	(%)	(kN/m)	(%)	(kN)	(%)	
H/Lw = 1	Capacity curve (without considering the masonry)	558.927	-	166,181.778	-	450.876	-
	Capacity curve (considering masonry with $f'm = 1$ MPa)	558.932	0.00	166,221.205	0.024	450.880	0.00
	Capacity curve (considering masonry with $f'm = 10$ MPa)	558.932	0.00	166,552.874	0.223	450.880	0.00
	Capacity curve (considering masonry with $f'm = 30$ MPa)	558.932	0.00	167,171.707	0.596	450.880	0.00
H/Lw = 3	Capacity curve (without considering the masonry)	186.309	-	6504.788	-	150.292	-
	Capacity curve (considering masonry with $f'm = 1$ MPa)	186.311	0.00	6506.331	0.024	150.293	0.00
	Capacity curve (considering masonry with $f'm = 10$ MPa)	186.311	0.00	6519.314	0.223	150.293	0.00
	Capacity curve (considering masonry with $f'm = 30$ MPa)	186.311	0.00	6543.536	0.596	150.293	0.00

### 3.2.3. Benchmark Capacity Curves vs. Experimental Tests

The benchmark capacity curves obtained with the assumptions and procedures described in this document should be compared against experimental data. For this matter, the tests developed by Albuja and Pantoja [18] were used to verify the reliability of this study’s analytical benchmark capacity curves. Figure 21 presents the comparison between the experimental and benchmark capacity curves. Different limit states such as yielding, serviceability, and damage control are included in Figure 21 to compare the estimations of the benchmark capacity curves based on the magnitude of the lateral displacement.



**Figure 21.** Benchmark and experimental capacity curves comparison.

In Figure 21, it is observed that the benchmark capacity curve may address displacements that are smaller than the damage control limit state. Nevertheless, the difference in the capacity curves for displacements beyond damage control may occur for failure modes other than flexural failure. For example, Albuja and Pantoja [18] describe the occurrence of torsional displacement at the ultimate stages of the test. Thus, more experimental tests are required to understand the limitations of the benchmark capacity curves of this study. Table 6 presents the difference in percentage between the experimental results and the benchmark capacity curves in terms of maximum strength and stiffness. The variations presented in Table 6 indicate that the benchmark capacity curves may be used to calibrate computational models without additional experimental data.

**Table 6.** Summary of comparison between benchmark capacity curve and experimental capacity curve.

Case of Study	Stiffness	Error	Maximum Strength at Serviceability	Error	Maximum Strength at Control Strain 2	Error
	(kN/m)	(%)	(kN)	(%)	(kN)	(%)
Benchmark capacity curve	122,116.13		313.57		332.94	
Experimental capacity curve	121,876.04	0.20	304.06	3.13	314.53	5.85

### 3.3. Model Calibration

Figure 22 compares the capacity curves obtained from computational models versus benchmark capacity curves (for the different wall height discretizations and H/Lw values). In all the cases, the wall without discretization presents the worst prediction, and discretized walls with intermediate rigid links improve the estimation. For example, walls without discretization underestimate maximum strength, stiffness, and residual strength. As presented in Figure 22, these prediction issues are reduced by discretizing and including intermediate rigid links throughout the wall height.

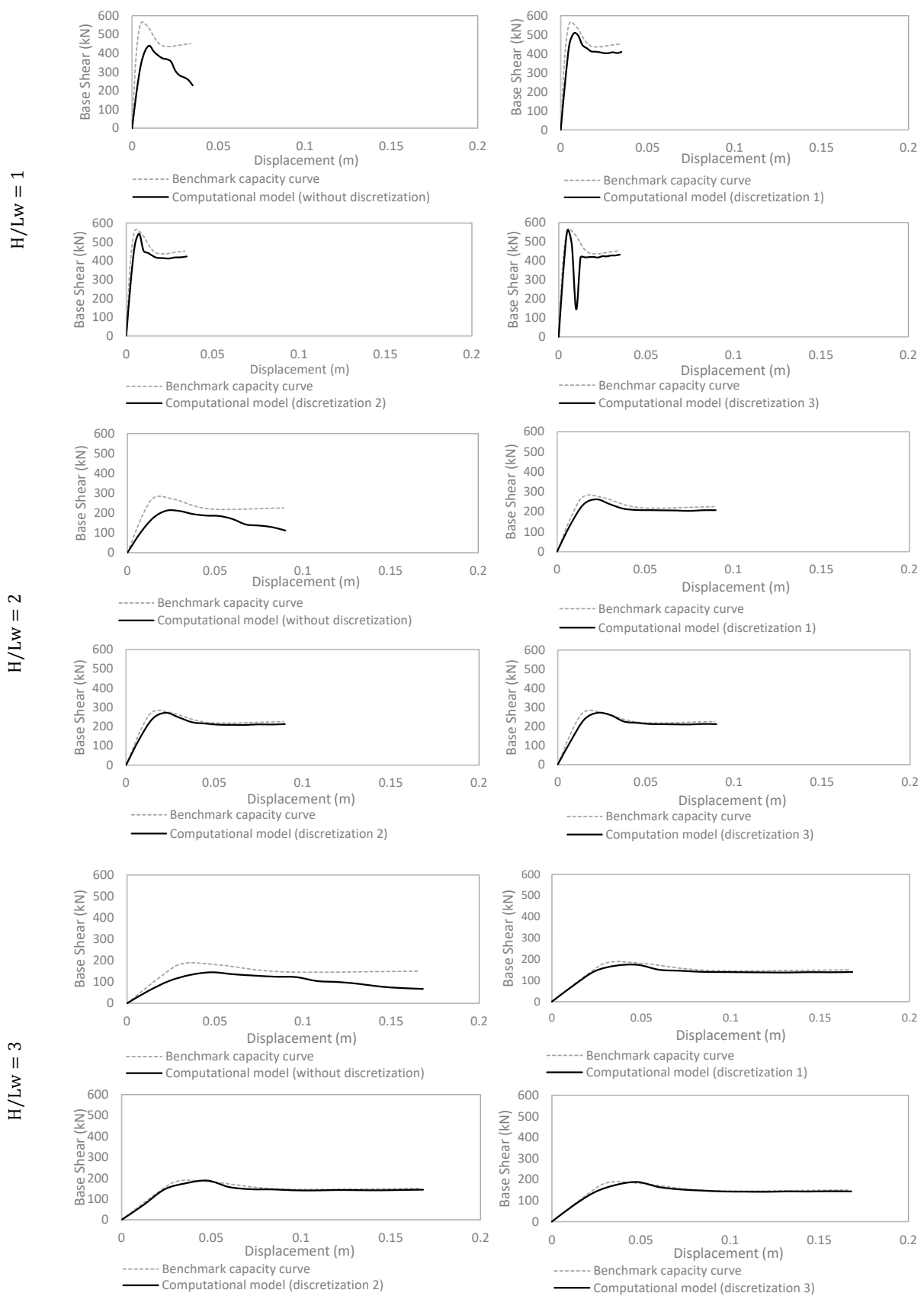


Figure 22. Capacity curves for each  $H/L_w$ .

For walls with  $H/L_w = 2$  and  $3$ , Figure 22 shows qualitatively that discretization 1, 2, and 3 present similar improvements. On the other hand, short walls ( $H/L_w = 1$ ) may improve the estimation only for discretizations 1 and 2. Discretization 3 can have convergence issues, which cause jumps in the capacity curve. The short wall ( $H/L_w = 1$ ) with discretization 3 has wall elements of 0.65 m in height and 2.1 m in length, resulting in a small aspect ratio of 0.3. Therefore, discretizing elements with a small aspect ratio can produce convergence issues.

In addition, Table 7 presents a quantitative summary of differences in relative percentage between the benchmark and computational capacity curves for parameters like maximum strength, initial stiffness, and residual strength. The maximum relative errors are 24.01%, 59.6%, and 55.09%, respectively. After including the intermediate rigid links, the initial stiffness parameter, which had the largest error, improved from 59.6% to 6.49%. On the other hand, the maximum strength, which had the smallest error range, improved from 24.01% to 0.32%. In general, the wall with  $H/L_w = 1$  had larger errors compared to the wall with  $H/L_w = 3$ , which had the smallest errors. Based on the relative errors presented in Table 7, there were significant improvements in the prediction by adding one intermediate rigid link. Additionally, Table 7 shows that discretizations 2 and 3, in most cases, can slightly improve the predictions made with discretization 1.

**Table 7.** Summary of differences in relative percentage between the benchmark and computational capacity curves.

Case of Study	Maximum Strength	Error	Stiffness	Error	Residual Strength	Error	
	(kN)	(%)	(kN/m)	(%)	(kN)	(%)	
$H/L_w = 1$	Benchmark capacity curve	558.93	-	166,185.41	-	450.88	-
	Model without discretization	439.73	21.33	67,138.20	59.60	227.91	49.45
	Model with discretization 1	507.27	9.24	90,077.46	45.80	409.85	9.10
	Model with discretization 2	543.22	2.81	97,038.72	41.61	422.50	6.29
	Model with discretization 3	560.69	0.32	112,138.88	32.52	432.04	4.18
$H/L_w = 2$	Benchmark capacity curve	279.46	-	21,649.63	-	225.44	-
	Model without discretization	212.37	24.01	11,829.18	45.36	111.83	50.40
	Model with discretization 1	261.79	6.33	15,737.77	27.31	207.48	7.97
	Model with discretization 2	271.65	2.80	16,025.25	25.98	213.24	5.41
	Model with discretization 3	271.12	2.99	15,707.89	27.45	211.96	5.98
$H/L_w = 3$	Benchmark capacity curve	186.31	-	6504.93	-	150.29	-
	Model without discretization	145.64	21.83	4378.05	32.70	67.49	55.09
	Model with discretization 1	173.54	6.85	5973.42	8.17	139.72	7.04
	Model with discretization 2	187.44	0.61	6082.98	6.49	144.08	4.13
	Model with discretization 3	188.11	0.97	5821.39	10.51	143.44	4.56

#### 4. Discussion

Current construction codes require detailed analyses for structural retrofitting considering the performance during seismic events. Therefore, the computational models used to evaluate existing infrastructure require nonlinear structural analysis and damage estimates. For structural retrofitting, nonlinear computational modeling is a widely used tool, but it must represent the connectivity between existing and new elements. This study proposes recommendations on the structural modeling of fiber elements to represent reinforced concrete (RC) moment frames retrofitted with mortar walls reinforced with steel wire mesh.

A key finding of this study was that modeling these retrofitted moment frames with insufficient connectivity nodes and constraint conditions leads to the inaccurate estimation of capacity curves. SeismoStruct computational models do not have the option to define shear wall transverse sections with different materials for border and web sections, so the retrofitted shear wall was defined with individual border and web elements, which are connected by default program options. This study found that insufficient connectivity and

constraint conditions produce issues in the capacity curve prediction, like underestimating maximum strength, initial stiffness, and residual strength. Improving the modeling of these systems was required to better evaluate the performance of the existing moment frames retrofitted with mortar walls reinforced with steel wire mesh.

Since the capacity curves are a primary tool for performance-based design and assessment, accurate predictions using computational models are critical for implementation. In general, there are standard procedures and models that work well for typical systems (moment frames and shear walls), but new systems (like the one presented in this study) cannot use the same procedure for standard systems. Therefore, the computational models for nonstandard systems must be calibrated to achieve accurate and reliable results.

This study identifies an easy solution to reduce issues in capacity curve predictions for fiber computational models of moment frame systems retrofitted with mortar walls reinforced with steel wire mesh. By including at least one intermediate rigid link constraint at mid-height on the shear wall, the capacity curves improve in terms of maximum strength, initial stiffness, and residual strength (for quantitative improvement values, see Table 7). By applying the recommendations of this study, more complex models like 3D structures may estimate better capacity curves, and the data obtained from those analyses will be reliable. However, it is also recommended that the results obtained in this study may be validated with future experimental studies.

This study is limited to the following assumptions: the integrity between moment frame and mortar wall is accomplished with sufficient steel rods, the shear strength of mortar wall web is larger than the retrofit wall flexural strength (shear failure is pre-vented), the masonry shear deformations do not contribute to large displacements, and the mortar wall shear displacements are elastic. Therefore, the estimations made with this study's benchmark capacity curves and computational fiber models require additional verifications with further experimental data to improve assessments of real failure modes observed after strong earthquakes. Future research should address failure modes like wall shear failure, mortar wall web concrete crushing, reinforcement buckling, steel rod slip at connectivity interfaces, and wall out-of-plane displacements.

## 5. Conclusions

For structural retrofitting, nonlinear computational modeling is a widely used tool, but it needs to represent the connectivity between existing and new elements. Therefore, the computational models for moment frames retrofitted with mortar walls reinforced with steel wire mesh require calibration to obtain reliable capacity curves.

This study found that using a single wall element connecting top and bottom frame border elements with rigid link constraint conditions underestimates maximum strength, stiffness, and residual strength in the capacity curve of this type of retrofit.

It is proposed to include at least one intermediate connectivity node at the wall mid-height, where the lateral columns are connected to the wall with rigid links. This approach improves the prediction of the capacity curve because it better represents the Bernoulli–Euler beam theory (the plane sections remain plain).

The calibrated wall with  $H/L_w = 1$  is the one with larger errors, and the wall with  $H/L_w = 3$  has smaller errors. Based on the relative errors obtained in this study, significant improvements in the capacity curve predictions were observed by just adding one intermediate rigid link. Moreover, by including more than one intermediate rigid link, it results in slight improvement from the previous prediction.

Applying the procedure presented in this study for wall discretizations corresponding to elements with an aspect ratio close to 0.3 will produce convergence issues.

**Author Contributions:** Conceptualization, M.H., D.S. and S.D.; methodology, M.H.; software, M.H.; validation, D.S., J.T. and S.D.; formal analysis, M.H., J.T. and D.S.; investigation, M.H.; resources, D.S. and J.T.; data curation, M.H.; writing—original draft preparation, M.H. and D.S.; writing—review and editing, M.H., D.S., J.T. and S.D.; visualization, M.H., J.T. and D.S.; supervision, D.S., J.T. and S.D.; project administration, M.H. and D.S.; funding acquisition, M.H., D.S. and S.D. All authors have read and agreed to the published version of the manuscript.

**Funding:** Escuela Politécnica Nacional.

**Institutional Review Board Statement:** Not applicable.

**Informed Consent Statement:** Not applicable.

**Data Availability Statement:** Not applicable.

**Conflicts of Interest:** The authors declare no conflict of interest.

## References

1. Gombosuren, D.; Maki, T. Effect of Joint Flexibility on Seismic Performance of a Reinforced Concrete Ductile Moment-Resisting Frame. *Adv. Mater. Sci. Eng.* **2022**, *2022*, 6858283. [[CrossRef](#)]
2. Wararuksajja, W.; Srechai, J.; Leelataviwat, S. Seismic design of RC moment-resisting frames with concrete block infill walls considering local infill-frame interactions. *Bull. Earthq. Eng.* **2020**, *18*, 6445–6474. [[CrossRef](#)]
3. Hidalgo, P.A.; Ledezma, C.A.; Jordan, R.M. Seismic behavior of squat reinforced concrete shear walls. *Earthq. Spectra* **2002**, *18*, 287–308. [[CrossRef](#)]
4. Ricci, I.; Palermo, M.; Gasparini, G.; Silvestri, S.; Trombetti, T. Results of pseudo-static tests with cyclic horizontal load on cast in situ sandwich squat concrete walls. *Eng. Struct.* **2013**, *54*, 131–149. [[CrossRef](#)]
5. Ozkul, T.A.; Kurtbeyoglu, A.; Borekci, M.; Zengin, B.; Kocak, A. Effect of shear wall on seismic performance of RC frame buildings. *Eng. Fail. Anal.* **2019**, *100*, 60–75. [[CrossRef](#)]
6. Wei, F.; Chen, H.; Xie, Y. Experimental study on seismic behavior of reinforced concrete shear walls with low shear span ratio. *J. Build. Eng.* **2022**, *45*, 103602. [[CrossRef](#)]
7. Arroyo, O.; Feliciano, D.; Carrillo, J.; Hube, M.A. Seismic performance of mid-rise thin concrete wall buildings lightly reinforced with deformed bars or welded wire mesh. *Eng. Struct.* **2021**, *241*, 112455. [[CrossRef](#)]
8. Blandon, C.A.; Arteta, C.A.; Bonett, R.L.; Carrillo, J.; Beyer, K.; Almeida, J.P. Response of thin lightly-reinforced concrete walls under cyclic loading. *Eng. Struct.* **2018**, *176*, 175–187. [[CrossRef](#)]
9. Carrillo, J.; Vargas, D.; Sánchez, M. Stiffness degradation model of thin and lightly reinforced concrete walls for housing. *Eng. Struct.* **2018**, *168*, 179–190. [[CrossRef](#)]
10. Alcocer, S.M.; Ruiz, J.; Pineda, J.A.; Zepeda, J.A. Retrofitting of Confined Masonry Walls with Welded Wire Mesh. In Proceedings of the Eleventh World Conference on Earthquake Engineering, Acapulco, Mexico, 23–28 June 1996; pp. 1–8.
11. Carrillo, J.; Pincheira, J.A.; Flores, L.E. Quasi-static cyclic tests of confined masonry walls retrofitted with mortar overlays reinforced with either welded-wire mesh or steel fibers. *J. Build. Eng.* **2020**, *27*, 100975. [[CrossRef](#)]
12. Fardis, M.N.; Schetakis, A.; Strepelias, E. RC buildings retrofitted by converting frame bays into RC walls. *Bull. Earthq. Eng.* **2013**, *11*, 1541–1561. [[CrossRef](#)]
13. Frosch, R.J.; Li, W.; Jirsa, J.O.; Kreger, M.E. Retrofit of Non-Ductile Moment-Resisting Frames Using Precast Infill Wall Panels. *Earthq. Spectra* **1996**, *12*, 741–760. [[CrossRef](#)]
14. Priestley, M.J.N.; Calvi, G.M.; Kowalsky, M.J. *Displacement-Based Seismic Design of Structures*, 2nd ed.; Eucentre: Pavia, Italy, 2017.
15. Seismosoft SeismoStruct 2022—A Computer Program for Static and Dynamic Nonlinear Analysis of Framed Structures. 2022. Available online: <https://seismosoft.com/> (accessed on 21 March 2023).
16. Paulay, T.; Priestley, M.J.N. *Seismic Design of Reinforced Concrete and Masonry Buildings*; Wiley: New York, NY, USA, 1992; Volume 768.
17. Pachano, F. Determinación de Parámetros Mecánicos para Modelos no Lineales de Mampostería de Relleno en Pórticos de Hormigón Armado Obtenidos de Manera Experimental. Master’s Thesis, Escuela Politécnica Nacional, Quito, Ecuador, 2018.
18. Albuja Jaramillo, D.R.; Pantoja Taez, J.X. Estudio del Reforzamiento de la Mampostería de Bloque de Hormigón con Malla Electrosoldada Mediante Ensayos Destructivos. Bachelor’s Thesis, Escuela Politécnica Nacional, Quito, Ecuador, 2017.
19. Mander, J.B.; Priestley, M.J.N.; Park, R. Theoretical Stress-Strain Model for Confined Concrete. *J. Struct. Eng.* **1988**, *114*, 1804–1826. [[CrossRef](#)]
20. Martínez-Rueda, J.E.; Elnashai, A.S. Confined concrete model under cyclic load. *Mater. Struct.* **1997**, *30*, 139–147. [[CrossRef](#)]
21. Menegotto, M.; Pinto, P.E. Method of analysis for cyclically loaded R.C. plane frames including changes in geometry and non-elastic behaviour of elements under combined normal force and bending. *IABSE* **1973**, 15–22. [[CrossRef](#)]

**Disclaimer/Publisher’s Note:** The statements, opinions and data contained in all publications are solely those of the individual author(s) and contributor(s) and not of MDPI and/or the editor(s). MDPI and/or the editor(s) disclaim responsibility for any injury to people or property resulting from any ideas, methods, instructions or products referred to in the content.